




Changes in dynamic transitions between integrated and segregated states underlie visual hallucinations in Parkinson's disease

Angeliki Zarkali ^{1✉}, Andrea I. Luppi ^{2,3}, Emmanuel A. Stamatakis ^{2,3}, Suzanne Reeves⁴, Peter McColgan⁵, Louise-Ann Leyland¹, Andrew J. Lees⁶ & Rimona S. Weil^{1,7,8}

Hallucinations are a core feature of psychosis and common in Parkinson's. Their transient, unexpected nature suggests a change in dynamic brain states, but underlying causes are unknown. Here, we examine temporal dynamics and underlying structural connectivity in Parkinson's-hallucinations using a combination of functional and structural MRI, network control theory, neurotransmitter density and genetic analyses. We show that Parkinson's-hallucinators spent more time in a predominantly Segregated functional state with fewer between-state transitions. The transition from integrated-to-segregated state had lower energy cost in Parkinson's-hallucinators; and was therefore potentially preferable. The regional energy needed for this transition was correlated with regional neurotransmitter density and gene expression for serotonergic, GABAergic, noradrenergic and cholinergic, but not dopaminergic, receptors. We show how the combination of neurochemistry and brain structure jointly shape functional brain dynamics leading to hallucinations and highlight potential therapeutic targets by linking these changes to neurotransmitter systems involved in early sensory and complex visual processing.

¹ Dementia Research Centre, University College London, 8-11 Queen Square, London WC1N 3AR, UK. ² Division of Anaesthesia, School of Clinical Medicine, University of Cambridge, Cambridge CB2 0QQ, UK. ³ Department of Clinical Neurosciences, University of Cambridge, Cambridge CB2 0QQ, UK. ⁴ Division of Psychiatry, University College London, 149 Tottenham Court Rd, London W1T 7BN, UK. ⁵ Huntington's Disease Centre, University College London, Russell Square House, London WC1B 5EH, UK. ⁶ Reta Lila Weston Institute of Neurological Studies, University College London, 1 Wakefield Street, London WC1N 1PJ, UK. ⁷ Wellcome Centre for Human Neuroimaging, University College London, 12 Queen Square, London WC1N 3AR, UK. ⁸ Movement Disorders Consortium, University College London, London WC1N 3BG, UK. ✉email: a.zarkali@ucl.ac.uk

Psychotic disorders cause significant global burden to affected individuals, families and healthcare systems. In Parkinson's disease (PD), psychosis is common, and visual hallucinations are associated with cognitive decline¹, poorer quality of life² and increased mortality³. However, despite their impact, the brain changes that give rise to psychotic hallucinations are not fully understood. The transient, unpredictable nature of hallucinations, even in patients who regularly experience them, suggests they relate to changes in dynamic brain processes and shifts in states. Resting-state functional MRI (rsfMRI) measures spontaneous fluctuations in brain activity based on correlated fluctuations in blood oxygenation⁴ and has shown changes in the relative activity of specific functional brain networks in patients with PD-hallucinations⁵, with increased activation of the default mode network (DMN) and impaired recruitment of the dorsal attention network^{6–9}. However, these studies only provide a static image of functional connectivity, calculated over an entire scanning period, rather than examining dynamic changes in brain states.

An extension of this approach is dynamic functional connectivity analysis, which measures spontaneous fluctuations in connectivity over time^{10–12} and may be a more accurate representation of fluctuating cognitive states than previous static approaches¹³. Changes in temporal dynamics are seen in schizophrenia and other psychiatric conditions^{14–17}, and recent work showed imbalance of temporal dynamics of integrated and segregated states in anaesthesia and disorders of consciousness^{18,19} and after administration of the psychedelic LSD, known for its hallucinogenic properties²⁰. Changes in dynamic functional connectivity are described in PD²¹ and are associated with severity of both motor and cognitive symptoms^{22–24} but are as yet unexplored in relation to neuropsychiatric symptoms.

Functional connectivity is likely to be affected by breakdown in the anatomical connections between regions. Indeed, PD patients with hallucinations show widespread disruption in structural connections between brain regions, measured using diffusion MRI^{25,26}. These changes particularly affect highly connected brain regions or “hubs” important for switching the brain between different states^{27,28}. Network control theory is a mathematical framework developed to study how the activity of a network's nodes is influenced by the network's structure. In the context of neuroscience, it offers a mechanistic explanation of how the brain transitions between cognitive states based on its structure, enabling behaviour²⁹. It integrates information from an individual's structural connectome (white matter connectivity derived from diffusion-weighted imaging) and temporal activation patterns (derived for example from fMRI) to specify how observed temporal activation patterns are constrained by the structural connectome^{29,30}. This framework defines brain states as the magnitude of haemodynamic activity across brain regions at a single time point and assumes that the brain's activation state at a given time is a linear function of a previous state, the underlying structural connectome and the additional control energy that is added to the system^{29,31}. In this way, the minimal energy cost needed to move the brain from one state to another can be calculated based on its structural network^{29,31,32}. A state that is less energy-demanding to maintain, or requires lower energy for transition, will be preferred. Recent work has shown that certain state transitions are preferable in the resting brain over others but this can be overcome by cognitive demands and is related to brain development and cognition^{33–36}. This framework has the potential to explain why a particular state is predominantly seen in health and how the balance between states may change in the presence of disease.

Transitions between functional states may be modulated by neurotransmitter systems³⁷. Dopamine transmission, particularly

D2 receptor expression guides state transitions during a working memory task³⁴. Excess dopamine release is a core neurobiological theory of schizophrenia³⁸, and excess striatal dopamine has been linked to hallucinatory experiences³⁹. Dopamine has long been considered the key driving neurotransmitter for PD hallucinations⁴⁰ with higher daily levodopa doses associated with higher risk of hallucinations^{41,42}. However, recent studies have challenged this model and implicated other neurotransmitters in PD-hallucinations: higher density of 5HT2A serotonin receptors⁴³, reduced GABA concentration⁴⁴ and cholinergic neuronal loss⁴⁵ have each been described in patients with PD and visual hallucinations. The role of dopamine in cognitive state transitions in health has also been challenged, with regional expression patterns of inhibitory and facilitatory neurotransmitters other than dopamine recently linked to dynamic functional states⁴⁶ and both noradrenaline^{12,47} and serotonin³⁷ driving whole-brain functional connectivity changes. A better understanding of the complex changes in neurotransmitter systems causing hallucinations would inform the development of more effective and targeted treatments for this distressing symptom.

Here, we aimed to investigate the nature of temporal dynamics in PD-associated visual hallucinations using rsfMRI; and determine whether the balance between predominantly Integrated and Segregated states of functional connectivity is altered in PD patients with hallucinations compared to patients without hallucinations and controls (overview in Fig. 1). We found that PD patients with hallucinations show impaired temporal dynamics, with a predisposition towards a predominantly Segregated state of functional connectivity. We then applied network control theory to calculate each individual's required energy cost to transition from the integrated-to-the-segregated state and vice versa, and the cost to maintain each state. We found that Parkinson's-hallucinators required less energy to transition from the integrated-to-segregated state than those without hallucinations and controls. Finally, we identified the brain regions that contribute most to the transition from integrated-to-segregated state. As dynamic neural systems are modulated by neurotransmitter systems^{37,47} we related the spatial organisation of this transition to regional neurotransmitter distribution using PET-derived density profiles and regional gene expression for neurotransmitter receptors.

Results

Ninety-one patients with PD were included: 16 PD patients with habitual visual hallucinations (PD-VH), 75 PD patients without hallucinations (PD-non-VH) and 32 controls. Demographics and clinical assessments are seen in Table 1. All participants experienced hallucinations in the visual domain, with details on the experienced hallucinatory images in Table 2. PD-VH and PD-non-VH were well matched in demographics, cognitive and motor performance, levodopa equivalent dose, and image quality and motion parameters (Table 1 and Supplementary Table 1). PD-VH participants showed higher depression scores ($p = 0.032$) than PD-non-VH participants but well below the clinical threshold for depression (≥ 8). As a result of the presence of hallucinations and higher depression burden ($p = 0.014$), PD-VH participants showed higher total UPDRS scores, which assessed non-motor symptoms, but they did not differ in terms of motor severity or levodopa equivalent dose. Although disease duration differed between PD-VH and PD-non-VH participants ($p = 0.044$), there was no correlation between disease duration and temporal functional changes ($\rho = -0.110$, $p = 0.297$ between proportion of time spent in an *Integrated* vs *Segregated* state and disease duration in PD participants) therefore we did not correct for disease duration in our main comparisons of interest.

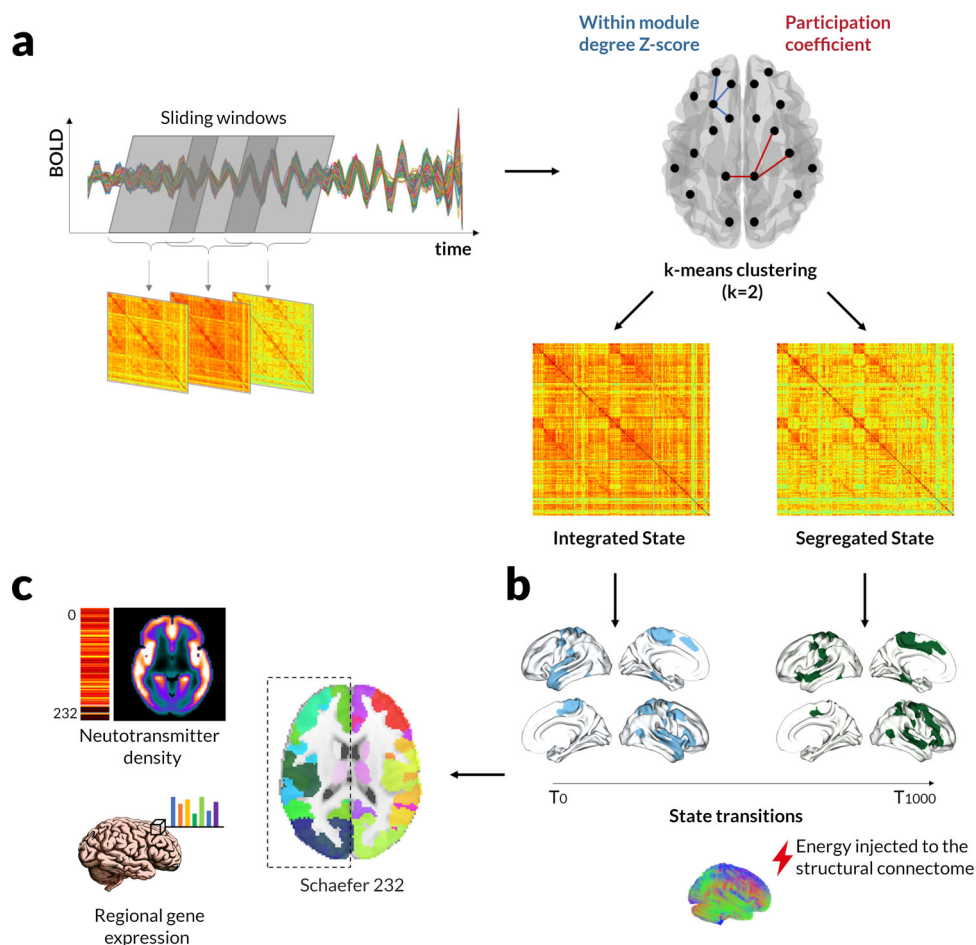


Fig. 1 Overview of the study methodology. **a** Deriving *Integrated* and *Segregated* states of dynamic functional connectivity. After obtaining sliding-windows (each 44 s duration) of dynamic functional connectivity for each participant, the joint histogram of participation coefficient and within-module degree Z-score was used for k -means clustering ($k = 2$) (BOLD, blood oxygen level dependent activity). The cluster with highest average participation coefficient is then identified as the predominantly *Integrated* dynamic state and the cluster with the lowest participation coefficient as the predominantly *Segregated* state. Note that this is done for each participant separately leading to individually-defined states. **b** Modelling state transitions. After deriving each individual's *Integrated* and *Segregated* states we used an optimal control framework to calculate the minimal control energy that needs to be applied to each node of the structural network to transition from a baseline state at time T_0 to a target state at time T_{1000} . Here, as an example, we illustrate the transition from the *Integrated* state (top 20% of nodes in blue) to the *Segregated* state (top 20% of nodes in green) but minimal energies were also calculated for segregated-to-integrated transition as well as minimal energies to maintain the *Integrated* state (integrated-to-integrated) and *Segregated* state (segregated-to-segregated) using the same model. Minimal control energies were calculated for each subject based on their structural brain network, which was estimated using diffusion imaging and probabilistic tractography. Both states were represented in the model as a vector of the sum connectivity strength for each node (1×232). **c** Linking with neurotransmitter systems. Minimal control energies to transition between and maintain functional states were compared between patients with PD with (PD-VH, $n = 16$) and without hallucinations (PD-non-VH, $n = 75$). Transitions that differed between groups were then further explored to examine whether contributing nodes (requiring mode control energy) were associated with specific neurotransmitter systems. To do this, we calculated for each of the 232 regions of interest of our parcellation (Schaefer 232: 200 cortical and 32 subcortical regions) (1) mean neurotransmitter density profiles derived from PET data (serotonin (*SHT1a*, *SHT2a* and *SHT1b*), dopamine (*D1* and *D2*) and GABA_A receptors) and (2) gene expression profiles for each of 31 pre-selected genes encoding receptors for norepinephrine, acetylcholine, dopamine and serotonin.

Preserved topology of functional connectivity states. To examine the dynamic changes in functional connectivity underlying PD-hallucinations, we employed an a priori clustering of dynamic functional connectivity into two states of functional connectivity, an *Integrated* and a *Segregated* state. After obtaining sliding-windows (44 s duration each) of dynamic functional connectivity for each participant, the joint histogram of participation coefficient and within-module degree Z-score for k -means clustering ($k = 2$; independently confirmed as optimal number of clusters on data-driven evaluation, Supplementary Fig. 1). The cluster with highest average participation coefficient was identified as the *Integrated* dynamic state and the cluster with the lowest participation coefficient as the *Segregated* state, as

previously described^{12,18,20,48,49}. This was performed separately for each participant (using the same criteria) leading to individually-defined *predominantly Integrated* and *Segregated* states (Fig. 1a). Differences between the two states are seen in Supplementary Fig. 2 and Supplementary Table 3.

These two states did not significantly differ between groups (PD versus controls or PD-VH versus PD-non-VH) when comparing connectivity strength in each state using network-based statistics, or between-group differences in density (*Integrated*: Kruskal–Wallis $H = 2.473$, $p = 0.290$, *Segregated*: 0.175, $p = 0.529$), entropy of connectivity values (*Integrated*: $H = 0.723$, $p = 0.696$, *predominantly-Segregated*: $H = 0.905$, $p = 0.636$), structural-functional coupling (*Integrated* $F(111,2) = 1.093$,

Table 1 Demographics and clinical assessments in patients with Parkinson's with hallucinations (PD-VH) and without hallucinations (PD-non-VH).

Attribute		Controls n = 32	PD-non-VH n = 75	PD-VH n = 16	p value
Demographics	Age (years)	66.1 (9.4)	64.4 (7.8)	64.8 (8.6)	0.653
	Male (%)	13 (40.6)	41 (54.7)	5 (31.2)	0.029 ^a
	Years in education	17.8 (2.5)	16.9 (2.6)	17.5 (3.6)	0.279
	Total intracranial volume (ml)	1390.7 (96.6)	1479.0 (132.6)	1407.3 (114.8)	0.002 ^a
Mood (HADS)	Depression score	1.7 (1.9)	3.9 (3.0)	4.7 (3.4)	0.032^{a,b,c}
	Anxiety score	4.0 (3.5)	5.6 (3.8)	7.0 (4.4)	<0.001 ^a
Vision	Visual acuity (LogMAR)*	-0.08 (0.23)	-0.08 (0.16)	-0.07	0.351
	Contrast sensitivity (Pelli Robson)*	1.78 (0.2)	1.79 (0.2)	1.70 (0.2)	0.106
	Colour vision (D15 total error score)	2.4 (6.9)	3.4 (8.7)	2.7 (4.6)	0.681
Cognition	MMSE	29.0 (1.0)	28.9 (1.2)	28.6 (1.9)	0.883
	MOCA	29.0 (1.3)	28.2 (2.1)	26.9 (3.4)	0.047 ^a
Attention	Digit span backwards	7.2 (2.1)	7.1 (2.3)	7.9 (2.3)	0.601
	Stroop: colour (sec)	32.1 (6.7)	33.5 (7.6)	38.1 (9.1)	0.089
Executive function	Stroop: interference (sec)	55.4 (11.6)	60.2 (19.2)	69.6 (23.9)	0.051
	Category fluency	22.5 (5.1)	21.7 (5.9)	19.8 (7.4)	0.339
Memory	Word Recognition Task	24.3 (1.2)	24.3 (1.2)	23.8 (0.9)	0.056
	Logical Memory	14.1 (4.1)	13.5 (4.3)	12.5 (4.6)	0.617
Language	Graded Naming Task	22.5 (6.2)	23.9 (2.9)	23.7 (2.3)	0.802
	Letter fluency	16.4 (5.4)	16.7 (5.4)	17.7 (5.3)	0.509
Visuospatial	Benton's Judgement of Line Orientation	24.9 (5.6)	24.5 (3.7)	23.1 (5.3)	0.338
	Hooper	25.7 (2.1)	24.7 (2.8)	23.3 (4.3)	0.074
	Disease-specific measures				
	Disease duration	-	3.9 (2.3)	5.3 (3.4)	0.044
	UPDRS total score	-	42.7 (20.8)	62.1 (38.5)	0.014
	UPDRS part 3 (motor)	-	21.2 (11.3)	29.8 (22.6)	0.129
	UM-PDHQ (hallucination severity score)	-	-	4.6 (2.4)	-
	LEDD (mg)	-	437.0 (255.1)	450.0 (221.2)	0.295
	RBDSQ	-	4.0 (2.4)	5.1 (2.5)	0.055

All data shown are mean (SD) except gender. In bold characteristics that significantly differed between the PD-VH and PD-non-VH. ^aSignificant difference between PD-VH and controls. ^bSignificant difference between PD-non-VH and controls. ^cSignificant difference between PD-VH and PD-non-VH. *Best binocular score used; LogMAR: lower score implies better performance, Pelli Robson: higher score implies better performance. HADS: Hospital anxiety and depression scale; MMSE: Mini-mental state examination; MOCA: Montreal cognitive assessment; UPDRS: Unified Parkinson's disease rating scale; UM-PDHQ: University of Miami Hallucination Questionnaire (max score: 14); LEDD: Total Levodopa equivalent dose; RBDSQ: REM sleep behaviour disorder screening questionnaire.

Table 2 Characteristics of visual hallucinations experienced by patients with Parkinson's disease (PD-VH).

Visual hallucinations characteristics	PD-VH (n = 16)
Phenotype	Complex visual hallucinations 11 (62.5%)
Frequency	Minor visual hallucinations 5 (31.3%)
	Less than once a week ^a 11 (62.5%)
Duration	More than once a week 5 (31.3%)
	Less than 1 s 8 (50.0%)
	Less than 10 s 6 (37.5%)
Insight	More than 10 s 2 (12.5%)
	Always preserved 10 (62.5%)
	Sometimes preserved 4 (25.0%)
Number of experienced images mean (sd)	No insight 2 (12.5%)
	1.44 (0.79)
Distress	10 (62.5%)
	Mild to moderate distress 6 (37.5%)

Participants were asked to reflect on all visual hallucinatory phenomena experienced within the previous month. Complex visual hallucinations included well-formed imagery (people, animals, etc.), stationary or animate images. Minor hallucinations included passage hallucinations and non-formed images (shadows, etc.). Misperceptions alone were not included as minor hallucinations. ^aAll participants experienced hallucinations more frequently than once per month.

$p = 0.339$, Segregated: $F(111,2) = 1.401$, $p = 0.251$) or small world propensity (Integrated: $H = 1.065$, $p = 0.587$, Segregated: $H = 4.400$, $p = 0.111$).

Impaired temporal properties of dynamic functional connectivity in patients with hallucinations. Although the states themselves did not differ between groups, we found significant changes in their temporal properties. PD-VH spent a significantly smaller proportion of time in the Integrated state (therefore more time in the Segregated state) than PD-non-VH ($\beta = -0.113$, $p = 0.032$) and controls ($\beta = -0.128$, $p = 0.026$) (Fig. 2a). Within PD patients, the proportion of time spent in the Integrated state was inversely correlated with hallucination severity (Spearman's $\rho = -0.259$, $p = 0.013$). Mean dwell time (number of consecutive windows spent in each state) in the Segregated state was higher in PD-VH than PD-non-VH (19.1 ± 16.9 in PD-VH vs 9.5 ± 9.1 in PD-non-VH $H = 4.058$, $p = 0.044$), but did not differ for the Integrated state ($H = 2.166$, $p = 0.141$). No differences were seen in dwell times of either state between PD and controls. Finally, the total number of transitions was lower in PD-VH than PD-non-VH (5.7 ± 5.3 in PD-VH vs 8.5 ± 6.2 in PD-non-VH, $H = 3.87$, $p = 0.049$) (Fig. 2b). Results were replicated using a finer parcellation (Supplementary Fig. 4). Overall, this suggests

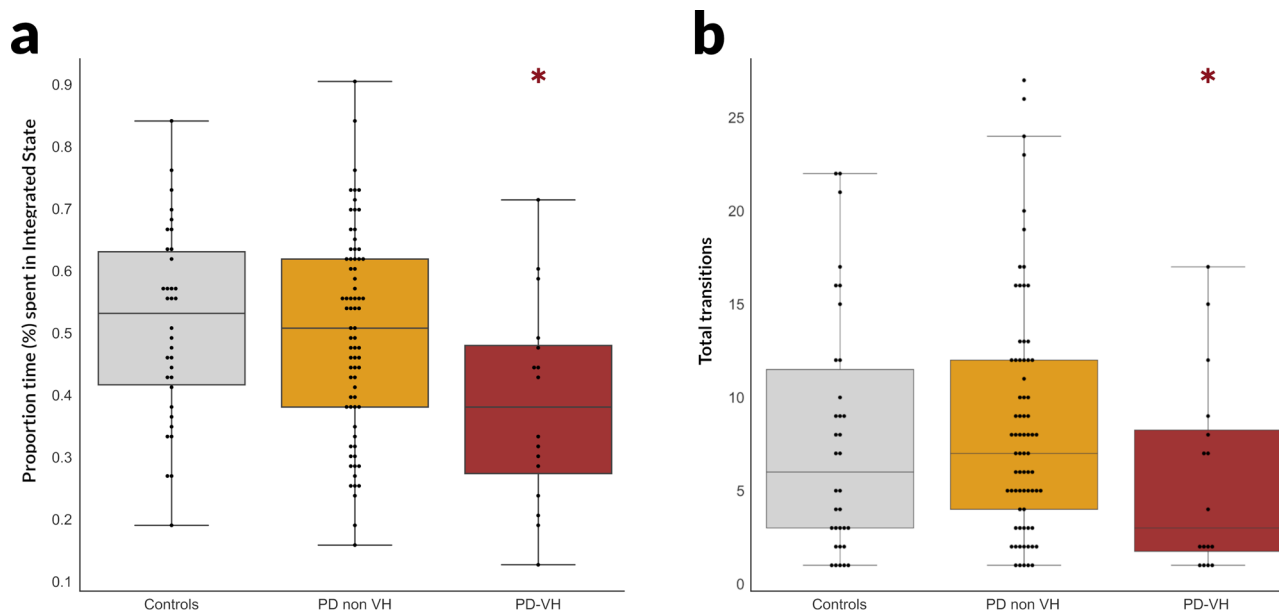


Fig. 2 Altered temporal properties of dynamic functional connectivity in patients with Parkinson's and visual hallucinations. **a** Percentage of total time spent in the *Integrated* state. Patients with Parkinson's with visual hallucinations ($n = 16$) spent significantly less time in the *Integrated* state of dynamic functional connectivity than patients without hallucinations ($n = 75$) ($p = 0.032$) and controls ($n = 32$) ($p = 0.0262$) (error bars are 95% confidence intervals). **b** Total number of transitions between states. Patients with Parkinson's and hallucinations ($n = 16$) had reduced overall transitions between states than patients without hallucinations ($p = 0.049$) (error bars are 95% confidence intervals). PD-VH: Parkinson's disease with visual hallucinations, PD-non-VH: Parkinson's disease without hallucinations.

that PD-VH spend more time in the *Segregated* state than PD-non-VH, with fewer total transitions and longer dwelling time within the *Integrated* state.

Reduced energy costs to transition from the integrated to segregated state in patients with visual hallucinations. Having identified significant differences in terms of brain dynamics between PD-VH and PD-non-VH, which are specifically related to the severity of visual hallucinations (the focus of our present investigation), we sought to interrogate further this difference between PD patients. We have previously shown widespread structural connectivity changes in PD-VH²⁸. Given neural dynamics are constrained by the structural connectome, we used the framework of network control theory to integrate information about structural network topology and functional brain dynamics^{29,31,32}. Using this framework, the minimal energetic cost to transition from one specific functional brain state (defined as the magnitude of brain activation at a specific time point) to another can be calculated using the structural brain network topology^{31,32,50}; lower energetic costs required to transition to a specific state may make this transition preferable.

Specifically, we aimed to investigate whether the *Segregated* state predominance observed in hallucinators could be explained by differences in ease of transition from the integrated-to-segregated state or vice versa or a difference in ease of maintaining the *Segregated* state. To do this, we calculated the minimal control energy that needs to be applied to the structural network of each participant to (1) transition from integrated-to-segregated state, (2) transition from segregated-to-integrated state, (3) maintain the *Integrated* state and (4) maintain the *Segregated* state (Fig. 1b). Minimal control energies were calculated for each subject based on their structural brain network, which was estimated using diffusion imaging and probabilistic tractography. For the purposes of this calculation, and in contrast to previous publications, we represented the *Integrated* and *Segregated* states as a vector of sum functional

connectivity for each brain region. We then examined whether transition and persistence energies in each state differed between PD-VH and PD-non-VH.

Similarly to previous work in healthy individuals³⁴, persistence energy for the more connected *Integrated* state was higher than the *Segregated* state for all participants (repeated measures ANOVA main effect of *Integrated* to *Segregated* state persistence energy $F(1,113) = 12.432$, $p < 0.001$). Similarly the minimal energy needed to transition from the *Segregated* to *Integrated* state was higher ($F(1,113) = 6.722$, $p = 0.011$) (Supplementary Fig. 3). When we examined differences between patients with PD with and without hallucinations, PD-VH needed significantly lower control energy to transition from the *Integrated*-to-*Segregated* state than PD-non-VH (effect size Hedge's $g = 0.922$, $t = 2.376$, $p = 0.029$) (Fig. 3a). There were no statistically significant differences between PD-VH and PD-non-VH in the minimal control energy needed to transition from *Segregated*-to-*Integrated* state ($t = 1.346$, $p = 0.195$), or to persist within the *Integrated* ($t = 1.041$, $p = 0.312$) or *Segregated* state ($t = 1.079$, $p = 0.295$). Therefore, network control theory reveals that the higher proportion of time that PD-VH patients spend in the *Segregated* state may be accounted for in terms of this state being easier to transition to from the *Integrated* state (as opposed to being easier to persist in).

Transition from integrated to the segregated state is driven by subcortical and more multimodal brain regions. A further benefit of applying control theory to functional brain states is that it provides regional information about the cost of maintaining and transitioning between these states.

We therefore aimed to identify which brain regions contribute more to this transition from the *Integrated*-to-*Segregated* state (which nodes require more energy in order to transition, with high contributors defined as the top 20% of regions). These higher contributors are more likely to be responsible for the changes in energy costs seen in PD-VH (significantly less control

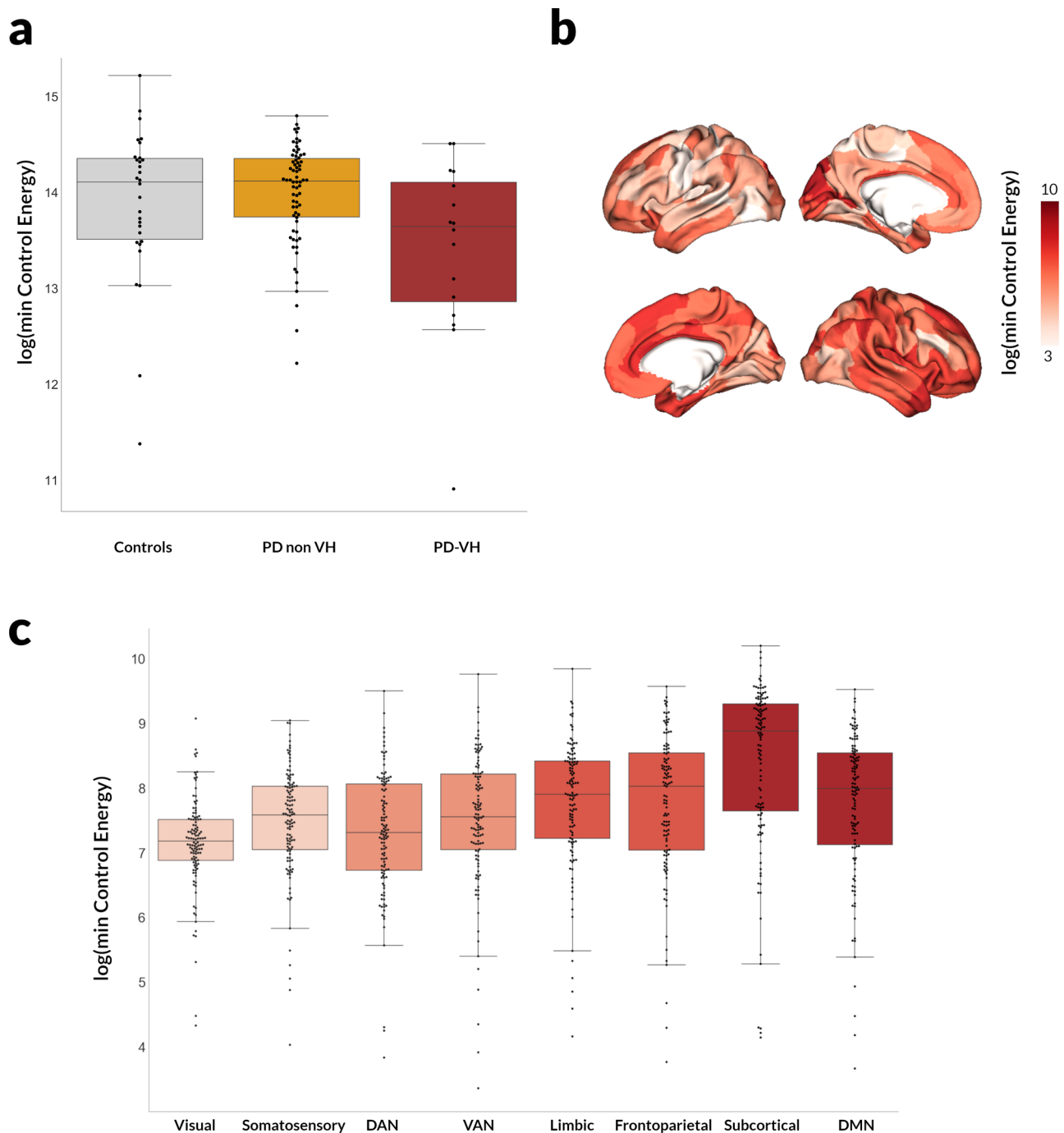


Fig. 3 Changes in control energy to transition from the *Integrated* to the *Segregated* state in patients with Parkinson's and visual hallucinations.

a Minimal control energy to transition from the *Integrated* to the *Segregated* state. Less energy is needed to transition for patients with Parkinson's and visual hallucinations (PD-VH, $n = 16$) than those without hallucinations (PD-non-VH, $n = 75$). Log-transformed minimal control energy is presented. Error bars are 95% confidence intervals. **b** Regional variation in minimal control energy to transition from the *Integrated* to the *Segregated* state. The log-transformed minimal control energy that needs to be applied to each node ($n = 232$ nodes) is presented; darker colours denote higher amounts of energy required. Note that only cortical regions are plotted. **c** Minimal control energy per functional subnetwork. The mean minimal control energy to transition from the *Integrated* to the *Segregated* state across all nodes ($n = 232$ nodes) of the seven cortical and one subcortical resting state networks is plotted. Darker colours denote higher levels of the cortical hierarchy; also left to right: unimodal to transmodal regions. There was a significant correlation between the minimal transition energy from integrated-to-segregated state that was needed to be applied to each node and the nodes position in the cortical hierarchy, with higher amount of energy needed for more transmodal regions ($\rho = 0.526$, $p < 0.001$). Error bars are 95% confidence intervals.

energy needed to transition from *Integrated*-to-*Segregated* state in PD-VH). As expected⁵¹, subcortical regions were strongly represented, with 25 subcortical nodes amongst the top 20% of contributors (25/47 or 53.2%) with thalamic regions amongst the highest contributors. Of the cortical nodes, top contributors

included predominantly right hemispheric regions (20/22 cortical nodes) including regions of the Default mode network: cingulum, precuneus, inferior and superior temporal regions and medial frontal regions (Table 3 and Fig. 3b). There was a significant correlation between the *Integrated*-to-*Segregated* state transition

Table 3 Top 20% of nodes that contribute to the transition from the *Integrated* to the *Segregated* state of dynamic functional connectivity.

Region	Coordinates in MNI space			Log(Energy) mean (std)	Network
	x	y	z		
<i>Cortical</i>					
Occipital_Mid_L	-22	-96	6	9.66 (8.49)	Visual
Cuneus_L	-12	-72	22	9.65 (8.49)	Visual
Temporal_Sup_R	64	-24	8	9.70 (8.35)	Somatosensory
Temporal_Sup_R	44	-28	18	9.72 (8.81)	Somatosensory
Rolandic_Oper_R	60	0	10	9.59 (8.60)	Somatosensory
Postcentral_R	58	-4	30	9.63 (8.54)	Somatosensory
Paracentral_Lobule_R	6	-22	68	9.94 (8.62)	Somatosensory
Cingulum_Mid_R	10	-36	46	9.38 (8.48)	VAN
Temporal_Inf_R	46	-12	-34	9.79 (8.38)	Limbic
ParaHippocampal_R	26	-10	-32	9.59 (8.38)	Limbic
SupraMarginal_R	62	-38	36	8.73 (8.76)	Frontoparietal
Temporal_Inf_R	62	-42	-12	9.38 (8.60)	Frontoparietal
Cuneus_R	14	-70	36	9.39 (8.60)	Frontoparietal
Cingulum_Mid_R	6	-24	30	8.99 (8.78)	Frontoparietal
Cingulum_Mid_R	4	2	30	7.97 (7.90)	Frontoparietal
Cingulum_Ant_R	8	30	28	7.64 (7.77)	Frontoparietal
Angular_R	50	-58	44	9.49 (8.50)	DMN
Rectus_R	4	36	-14	9.59 (8.38)	DMN
Cingulum_Ant_R	8	42	4	8.74 (8.94)	DMN
Frontal_Sup_Medial_R	8	58	18	5.07 (5.50)	DMN
Frontal_Mid_R	28	30	42	7.92 (8.18)	DMN
Precuneus_R	6	-58	44	9.24 (8.41)	DMN
<i>Subcortical</i>					
Anterior hippocampus R	26	-14	-20	9.55 (8.57)	Subcortical
Posterior hippocampus R	28	-32	-8	9.68 (8.87)	Subcortical
Lateral amygdala R	28	-2	-22	9.83 (8.30)	Subcortical
Medial amygdala R	22	-6	-16	5.49 (5.59)	Subcortical
Dorsoposterior thalamus R	16	-30	2	9.86 (8.64)	Subcortical
Ventroanterior thalamus R	8.0	-10.0	6.0	9.22 (8.67)	Subcortical
Dorsoanterior thalamus R	12.0	-22.0	12.0	8.57 (8.19)	Subcortical
Nucleus accumbens, shell R	12.0	10.0	-6.0	9.61 (8.68)	Subcortical
Nucleus accumbens, core R	14.0	18.0	-2.0	9.05 (8.53)	Subcortical
Posterior globus pallidus R	24.0	-8.0	-2.0	7.55 (8.16)	Subcortical
Posterior Putamen R	30.0	-6.0	4.0	5.15 (5.45)	Subcortical
Anterior Caudate R	14.0	14.0	6.0	8.05 (7.60)	Subcortical
Posterior Caudate R	14.0	4.0	16.0	9.89 (9.13)	Subcortical
Anterior hippocampus L	-24.0	-14.0	-20.0	8.15 (8.26)	Subcortical
Posterior hippocampus L	-26.0	-32.0	-8.0	9.32 (8.23)	Subcortical
Lateral amygdala L	-26.0	-2.0	-22.0	8.36 (8.29)	Subcortical
Medial amygdala L	-20.0	-6.0	-16.0	9.67 (8.64)	Subcortical
Dorsoposterior thalamus L	-14.0	-30.0	2.0	9.74 (8.39)	Subcortical
Ventroanterior thalamus L	-6.0	-10.0	6.0	8.22 (8.06)	Subcortical
Dorsoanterior thalamus L	-10.0	-22.0	12.0	7.47 (6.76)	Subcortical
Nucleus accumbens, shell L	-10.0	10.0	-6.0	7.66 (7.69)	Subcortical
Nucleus accumbens, core L	-12.0	18.0	-2.0	9.30 (8.50)	Subcortical
Posterior globus pallidus L	-22.0	-8.0	-2.0	7.30 (7.50)	Subcortical
Anterior Caudate L	-12.0	14.0	6.0	9.87 (8.63)	Subcortical
Posterior Caudate L	-12.0	4.0	16.0	6.89 (7.14)	Subcortical

L left, R right hemisphere.

energy required at each node and the node’s position in the cortical hierarchy, with higher energy needed for more transmodal regions ($\rho = 0.526, p < 0.001$) (Fig. 3c).

Correlation with neurotransmitter systems. Finally, we examined whether the *Integrated-to-Segregated* state transition (which was the state transition that specifically differed for PD-VH patients), is associated with specific neurotransmitter systems (Supplementary Table 2) in the healthy brain. To do this, we correlated the mean control per node to transition from the *Integrated-to-Segregated* state with mean regional neurotransmitter

density (derived from open-access PET data) and neurotransmitter receptor gene expression levels (derived from the Allen Brain atlas⁵²) in health; we tested this against spatially-correlated null models through sphere permutations, FDR-corrected for multiple comparisons over 232 nodes (Fig. 1c).

We found a significant correlation between regional log(Energy) and density of *5HT1b* ($\rho = -0.274, q_{spin} = 0.009$), *5-HT2a* ($\rho = -0.347, q_{spin} < 0.001$) and *GABA_A* receptors ($\rho = -0.317, q_{spin} = 0.022$), from open-access atlases of PET data (Fig. 4). Regional energy and regional expression levels of genes relating to 5-HT2a receptors were also significantly correlated ($\rho = -0.1438$,

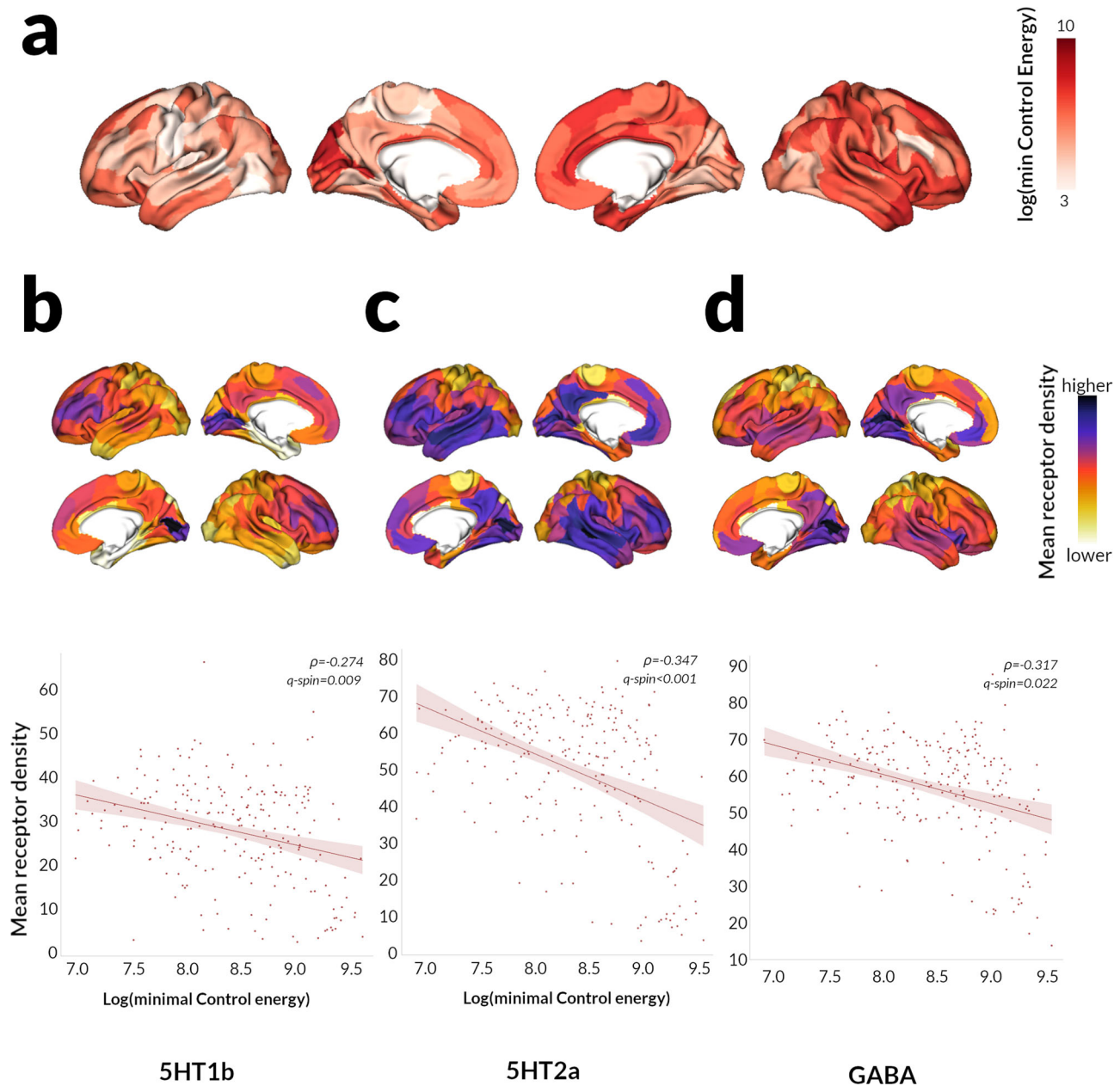


Fig. 4 Neurotransmitter correlates of Integrated-to-Segregated state transition. The log-transformed minimal control energy that needs to be applied to each node ($n = 232$ nodes) to achieve the Integrated-to-Segregated state transition (**a**) was correlated with the mean regional receptor density of 5HT1b receptors (**b**), 5HT2a receptors (**c**) and GABA receptors (**d**), from open access atlases of PET data in unaffected individuals. In all cases, ρ is the Spearman correlation coefficient and q -spin is the FDR-corrected p -value derived following spatial permutations (p -spin, 1000 permutations).

$q_{\text{spin}} = 0.044$) as well as two GABA_A receptors [GABRA1 ($\rho = -0.2437$, $q_{\text{spin}} = 0.020$) and GABRA2 ($\rho = 0.128$, $q_{\text{spin}} = 0.023$)]; gene expression data for 5-HT1b receptors were not available. Although noradrenergic and acetylcholinergic PET data are not publicly available, genetic expression of noradrenergic (*ADRA1B* and *ADRA2A*), muscarinic (*CHRM1*, *CHRM2*, *CHRM3*, *CHRM4*) and nicotinic receptors (*CHRNA3*, *CHRNA4*, *CHRNA7*, *CHRNA2*) was correlated with regional transition energy. Gene expression of DRD2 was also correlated with regional control energy for the *Integrated-to-Segregated* state transition ($\rho = 0.318$, $q_{\text{spin}} = 0.013$) but this was not replicated using density PET-derived data ($\rho = 0.056$, $q_{\text{spin}} = 0.800$). The detailed correlations between regional control energy and transmitter density and regional gene expression are seen in Table 4.

Discussion

We have used dynamic functional connectivity and network control theory to explore the temporal dynamics underlying visual hallucinations in Parkinson's, and examined how these can be explained through changes in brain structure. We found that PD-hallucinators spent more time in a *predominantly Segregated* state of functional connectivity than those without hallucinations, with fewer total transitions and longer dwelling time within the *Segregated* state. The transition from the *Integrated-to-Segregated* state was less energy-demanding in PD-hallucinators than non-hallucinators. This transition is mediated by transmodal brain regions that are associated with specific neurotransmitter systems, as confirmed through both in vivo PET mapping and post-mortem gene expression microarray data.

Table 4 Neurotransmitter receptors showing density and gene expression correlations with regional control energy required to transition from the *Integrated* to the *Segregated* state.

Receptor	Ligand	Correlation coefficient	q value
<i>Receptor density</i>			
5-HT1B	Serotonin	−0.274	0.009
5-HT2A	Serotonin	−0.347	0.000
GABA	GABA	−0.317	0.022
<i>Receptor gene expression</i>			
Gene symbol	Ligand	Correlation coefficient	q value
ADRA1B	Norepinephrine	−0.154	0.018
ADRA2A	Norepinephrine	−0.210	0.013
CHRM1	Acetylcholine	−0.279	0.018
CHRM2	Acetylcholine	−0.265	0.028
CHRM3	Acetylcholine	−0.223	0.018
CHRM4	Acetylcholine	0.202	0.018
CHRNA3	Acetylcholine	0.416	0.013
CHRNA4	Acetylcholine	−0.158	0.033
CHNRA7	Acetylcholine	−0.244	0.023
CHNRB2	Acetylcholine	0.207	0.028
DRD2	Dopamine	0.318	0.013
HTR1E	Serotonin	−0.207	0.013
HTR1F	Serotonin	−0.3301	0.013
HTR2A	Serotonin	−0.144	0.044
HTR5A	Serotonin	−0.311	<0.001
GABRA1	GABA	−0.244	0.020
GABRA2	GABA	0.128	0.023
GABRAB2	GABA	0.433	0.018
GABRAD	GABA	−0.289	0.013
GABRG1	GABA	0.227	0.023
GABRG2	GABA	−0.337	0.023
GABRG3	GABA	−0.217	0.044

Note that correlation coefficients of absolute values between 0.1 and 0.4 represent moderate correlation in our dataset. Q values are FDR-corrected p-values from spatial permutation testing (q-spin).

CHRNA nicotinic cholinergic receptor (Alpha), DRD dopamine receptor D, HTR 5-hydroxytryptamine receptor, ADRA alpha-1A adrenergic receptor, GABR GABA receptor.

Previous studies have shown that PD patients with cognitive impairment similarly spend more time in a Segregated state and show fewer transitions between states than PD with intact cognition and controls^{23,24}. There were no differences in cognitive performance between PD patients with and without hallucinations in our cohort, but visual hallucinations are known to be associated with incipient dementia in PD⁵³. In schizophrenia, where auditory hallucinations are a core feature, similar findings of altered dwell time are seen^{14,54}, correlated with severity of hallucinations⁵⁵. We similarly saw patients with visual hallucinations spending less time in the *Integrated* (and more time in the *Segregated*) state suggesting this finding may be specific to hallucinations as a trait.

We found that only the temporal dynamics of functional connectivity were altered in patients with hallucinations. This indicates that a change in the temporal balance between normal/preserved states rather than a change in the states themselves underlie PD-hallucinations. This contrasts with work using similar methodologies in patients with loss of consciousness and in healthy volunteers after LSD administration where within-state changes particularly within the *Integrated* state^{18,20}, were also seen. However, as we examined the propensity to hallucinate rather than the hallucinatory state itself (participants were not actively experiencing hallucinations during scanning) it is possible that additional within-state changes could underlie visual

hallucinations in PD, in the moment when they actually occur, an avenue for potential future investigations. In addition, although hallucinations in our participants were frequent (at least weekly in most participants) they were not universally complex and severe. Other important differences are that LSD-induced visual hallucinations are associated with changes in other sensory modalities including time/space dysperceptions and ego dissolution⁵⁶, which are not seen with PD-associated hallucinations; thus it is not unexpected that the underlying changes in temporal dynamics are different between these hallucinatory conditions.

As temporal transition between functional states is constrained by structural connectivity^{31,33,57}, we used network control theory to model the ease and regional contribution to the brain's activation for each of these two states, represented as the vector of sum connectivity for each region at each time point³¹. Specifically, we examined the energy cost of transitioning between and maintaining the *Integrated* and *Segregated* states. Minimisation of the control energy cost to transition into a state will make this transition more preferable, and evidence in healthy adolescents suggests lower control energy to activate the frontoparietal network during development (secondary to structural connectome reconfiguration) supports improved executive function³⁵. In addition, hallucination-inducing substances such as LSD and psilocybin have been recently shown to reduce overall control energy needed for between brain-state transitions leading to a more temporal labile functional landscape⁵⁸. We found a significantly lower energy cost to transition from the *Integrated*-to-*Segregated* state for PD-hallucinators than non-hallucinators. In this way, network control theory provides mechanistic insights about why patients with PD-VH spend more time in a more Segregated state: as it is more energy efficient to transition from the *Integrated*-to-*Segregated* state due to constraints caused by loss of structural integrity. Further, this framework enabled us to identify the particular nodes most critical in mediating these transitions, with subcortical (especially thalamic nodes) and regions within the DMN especially implicated, consistent with previous work highlighting DMN involvement in PD hallucinations⁶. Thalamic regions were amongst the highest contributors to this transition. Thalamic involvement has been previously described in visual hallucinations^{50,59} and we recently showed longitudinal changes in grey and white matter within the medial mediodorsal thalamus⁶⁰. This provides further evidence of the thalamus as a key driver of network imbalance in PD-hallucinations^{51,61}.

Interestingly, the brain regions contributing most to this transition from *Integrated*-to-*Segregated* state showed a correlation with specific neurotransmitter systems in health. Although the directionality of the relationship is difficult to interpret as data on regional neurotransmitter density and gene expression were derived from healthy individuals, regional density of *5HT2A* receptors was significantly correlated with the regional control energy needed for *Integrated*-to-*Segregated* state transition; this was replicated using regional expression data for the *5HT2A* receptor gene.

Activation of *5HT2A* receptors is a key mechanism for drug-induced hallucinations occurring with the psychedelic drugs, LSD, psilocybin and ayahuasca⁶² and modelling studies have shown that this receptor plays a key role in engendering the characteristic brain dynamics of LSD⁶³. Recent work highlighted the crucial role of *5HT2A* in neuronal-neurotransmission dynamic coupling across the brain³⁷. *5HT2A* has also been implicated in PD-hallucinations; evidenced by the higher density of *5HT2A* receptors within frontal, temporal and occipital regions in patients with PD hallucinations in post mortem and in vivo studies^{43,64} and the efficacy of the novel *5HT2A* inverse agonist

Pimavanserin in the treatment of PD-hallucinations⁶⁵. Visual hallucinations are a common phenomenological endpoint of both LSD and PD; our findings provide further evidence for the role of 5HT2A involved in PD-hallucinations, suggesting a convergent biological substrate across hallucinations irrespective of cause.

Other serotonergic receptors were also important for the *Integrated-to-Segregated* state transition including: 5HT1B (receptor density, but no genetic expression data), 5HT1E, 5HT1F and 5HT5A (gene expression data only). The correlation with multiple serotonin receptors, indicates that serotonergic modulators targeting multiple receptors could be potential therapeutic targets for PD-hallucinations. Of note, no receptor density or gene expression data were available for 5HT3 receptors, a target of interest for Ondansetron, a 5HT3-antagonist currently under evaluation as a treatment of hallucinations⁶⁶.

Regional receptor density and gene expression for GABAergic receptors were also correlated with regional transition energy in line with previous studies showing reduced GABA concentration in the visual cortex of PD-hallucinators^{44,67}. Visual processing involves a complex interplay between monoaminergic, cholinergic and GABA/glutamatergic neurotransmission⁶¹. The observed correlation between the *Integrated-to-Segregated* state transition and regional gene expression of noradrenergic (ADRA1B, ADRA2A) and cholinergic (muscarinic and nicotinic) receptors is consistent with this, but there were no available PET-derived density data to replicate this.

Convergent evidence has recently highlighted the importance of the noradrenergic system in some non-motor PD symptoms^{68–70}. Noradrenaline plays a key role in modulating selective attention⁷¹ and with serotonin, modulates behavioural responses to incoming visual information⁶¹. The noradrenergic system is also likely to play a key role in mediating functional state transitions: noradrenaline-mediated apical amplification of pyramidal cells differentiates waking and anaesthesia⁷², extracellular noradrenaline is associated with sleep-state transitions⁷³ and locus coeruleus activity flexibly mediates the recruitment of other neural circuits particularly the prefrontal cortex⁷⁴, leading to dynamic changes in functional networks, specifically transitioning between motor and task-negative networks⁷⁵. Changes within the noradrenergic system may be involved in altered state transitions in PD-hallucinations by modulating the activity of sensory cortices and thalamocortical neurocircuitry⁷⁶.

In contrast to these other neurotransmitters, we found no consistent correlation with dopaminergic receptors. It is important to note that although DRD1 is one of the major dopamine receptors in the cortex no DRD1 density data was publicly available at the time of the study; however, no correlation was seen between genetic expression of DRD1 and regional contribution to the *Integrated-to-Segregated* state transition. Although a lack of correlation between regional dopamine expression and regional energy does not exclude an indirect dopamine effect in visual hallucinations, our findings highlight the role of transmitters other than dopamine in the development of PD-hallucinations. Rather than a simple hyperdopaminergic state leading to PD-hallucinations, our findings suggest a complex imbalance in multiple neurotransmitter systems, with changes in 5HT2A, GABA and noradrenergic receptors all contributing. Treatment options targeting more than one neurotransmitter system may therefore be needed to manage visual hallucinations in PD and other psychotic illnesses.

Several considerations need to be taken into account when interpreting our findings. Our sample size of visual hallucinators is small, although comparable with other published studies^{24,27}. Functional data are susceptible to motion artefact; we adopted strict exclusion criteria to mitigate for this⁷⁷ and motion as well as

image quality metrics did not differ between groups. We chose not to perform global signal regression in keeping with other studies using the same analyses^{18,20}. Although this can be used to counteract residual artefacts from head motion⁷⁷ it can contain behaviourally-relevant information and affect group results^{78,79}, and we instead adopted stringent exclusion criteria for motion to limit potential motion effect. All participants were scanned while receiving their usual dopaminergic medications and at the same time of day and levodopa equivalent doses did not significantly differ between PD-VH and PD-non-VH⁸⁰. Further studies assessing PD patients ON and OFF levodopa might provide additional information. Although brain networks are non-linear, we used a linear optimal control model since this has been shown to provide important insights into non-linear dynamics⁸¹ and linear-Gaussian models are often adequate descriptors of functional MRI timeseries, such that more complex, non-linear models often do not provide additional explanatory power^{82,83}. Nevertheless, future work may seek to leverage insights from non-linear models of brain dynamics, e.g. through neurobiologically detailed *dynamic mean-field* models that have already been successfully applied to the study of altered states of consciousness^{63,84}. Most studies using network control theory so far have assessed transitions from rest to task³⁴ or activation of a specific functional network³⁵ where brain states are defined as regional activation by selecting which regions should be active or inactive. However, as our key question was to examine the transition between the integrated and segregated states (identified from the dynamic changes in the resting state timeseries from our patients), of dynamic functional connectivity in our patients, such an approach was not straightforwardly applicable in our case. Instead, in the literature on brain-states, it is common to define data-driven brain states in terms of time-resolved patterns of functional connectivity: that is, states are defined in terms of how regions are co-active together over a short period of time, rather than by specifying which regions should be active. Therefore, we used the sum of regional functional connectivity as a summary representation for each previously identified state; in this setting our activity states correspond to brief periods where specific nodes are active or inactive together, rather than nodes having high or low activity per se. In other words, our approach identifies states in terms of nodal co-activation. Although this approach provides insights into the relative ease of each transition, a task vs rest approach would be potentially even more informative and could be examined in future work. Finally, data on neurotransmitter density and gene expression were not derived from our participants but from separate cohorts of healthy volunteers and post-mortem human brains, respectively; therefore results relating to neurotransmitter receptors should be interpreted with caution. Future work may seek to replicate these results with each patient's own unique neurotransmitter receptor signature, which may offer individualised insights and the opportunity to assess the directionality of this relationship, as well as potential targets for pharmacological intervention.

Our findings describe that temporal functional dynamics are altered in PD-hallucinations, with a predisposition towards a *Segregated* state of functional connectivity. This segregated state predominance can be explained by a reduced energy cost to transition from the integrated-to-segregated state in PD patients with hallucinations compared to those without hallucinations. We have also clarified the neuromodulatory correlates of the integrated-to-segregated state transition in the healthy brain. These results provide mechanistic insights into visual hallucinations in PD with implications for other psychotic disorders. By linking these changes to neurotransmitter systems, our findings highlight possible therapeutic targets for hallucinations, a core symptom of psychosis.

Methods

Participants. 123 participants were included: 91 PD patients and 32 unaffected controls. The study was approved by the Queen's Square Ethics Committee and participants provided written informed consent. Patients with PD were classified as PD with visual hallucinations (PD-VH, $n = 16$) if they scored ≥ 1 in Question 2.1 of the Unified Parkinson's Disease Rating Scale (UPDRS); the rest were classified as PD-non-VH ($n = 75$). We collected additional information on severity, frequency and phenomenology of experienced hallucinations with the University of Miami Parkinson's Disease Hallucinations Questionnaire (UM-PDHQ)⁸⁵. General cognition was assessed using the Mini-Mental State Examination (MMSE) and Montreal Cognitive Assessment (MoCA)^{86,87}. In addition, domain-specific cognitive assessments with two tests per domain included: Attention: Digit span backwards⁸⁸, Stroop, Naming⁸⁹; Executive functions: Stroop Interference⁸⁹, Category fluency⁹⁰; Memory: Word Recognition Task⁹¹, Logical Memory⁸⁸; Language: Graded Naming Task⁹², Letter fluency⁹⁰, and Visuospatial: Benton's Judgement of Line⁹³, Hooper Visual Organization Test⁹³. Mood was assessed using the Hospital Anxiety and Depression Scale (HADS)⁹⁴. Disease-specific measures for PD included: motor assessment using the Movement Disorder Society UPDRS⁹⁵, smell: Sniffin' Sticks⁹⁶, and sleep: REM Sleep Behaviour Disorder Questionnaire (RBDsQ)⁹⁷. Levodopa equivalent daily doses (LEDD) were calculated for PD participants⁹⁸.

MRI data acquisition and preprocessing. Imaging data were acquired on the same 3T Siemens Prisma-fit scanner: rsfMRI: gradient-echo EPI, TR = 70 ms, TE = 30 ms, 105 volumes; diffusion-weighted (DWI): 64 directions (b -values: 50, 300, 1000, 2000). Scanning took place at the same time of day, with PD patients receiving their normal anti-Parkinsonian medication.

Both imaging modalities underwent rigorous quality assurance: The MRI quality control tool (MRIQC) was used to assess rsfMRI data⁹⁹. Participants were excluded if any of the following was met: (1) mean frame-wise displacement >0.3 mm, (2) any frame-wise displacement >5 mm, or (3) outliers $>30\%$ of the whole sample. This led to 12 participants being excluded (11 PD). Therefore, 91 patients with PD (16 PD-VH and 75 PD-non-VH) and 32 controls are included. Note that our sample includes patients that overlap with other reports from our centre. Slight differences in included patients are caused by exclusions such as head movement and quality control that differ between studies.

All volumes of raw DWI datasets were visually inspected and evaluated for artefact; only scans with <15 volumes containing artefacts¹⁰⁰ were included in subsequent structural analyses, resulting in further 5 PD and 2 control participants being excluded.

Preprocessing of rsfMRI data was performed as described previously¹⁰¹. In brief, we used fMRIPrep 1.5.0¹⁰² and discarded the first 4 volumes to allow steady-state equilibrium. Functional data were slice-time corrected using 3dTshift from AFNI¹⁰³ and motion corrected using mcflirt¹⁰⁴. Distortion correction was performed using TOPUP¹⁰⁵. This was followed by co-registration to the corresponding T1-weighted image using boundary-based registration with six degrees of freedom¹⁰⁶. Motion correcting transformations, field distortion correcting warp, BOLD-to-T1w transformation and T1w-to-template (MNI) warp were concatenated and applied in a single step using antsApplyTransforms (ANTs v2.1.0) using Lanczos interpolation. Physiological noise regressors were extracted applying CompCor¹⁰⁷. Spurious sources of signal were removed through linear regression: six motion parameters, mean signal from white matter and cerebrospinal fluid. We did not regress global signal given the lack of consensus and potential to distort group differences⁷⁸.

Preprocessing of diffusion-weighted images was performed in MRtrix3¹⁰⁸ using dwipreproc, with denoising¹⁰⁹, removal of Gibbs ringing artefacts¹¹⁰, eddy-current and motion correction¹¹¹ and bias field correction¹¹².

Parcellation. To construct functional and structural connectivity matrices, each participant's T1-weighted image was parcellated into 200 cortical and 32 sub-cortical regions of interest (ROIs) using the Schaefer¹¹³ and Tian parcellations¹¹⁴, respectively. Parcellations in the order of 200 regions result in connectomes with the highest representativeness^{115,116} and the combined Schaefer-232 parcellation used here, is considered optimal across structural and functional connectomes¹¹⁵. We used the same parcellation to construct functional and structural connectivity matrices for each participant. To ensure robustness of results, analyses were replicated using the finer-grained Schaefer/Tian parcellations with 400 cortical and 54 subcortical ROIs, respectively.

Dynamic functional connectivity analysis. Dynamic connectivity matrices were derived using an overlapping sliding-window approach¹⁰ with windows of 44 s duration (63^*TR , within the recommended range¹⁰) in steps of 1 repetition size (63 windows 44 s each) (Fig. 1a). A 232^*232 weighted adjacency matrix representing the functional connectome for that time point was calculated for each window.

We then identified states of higher integration or segregation using a "cartographic profile"^{12,18,20,117}. At each time point, the asymmetric algorithm of Rubinov and Sporns¹¹⁸ was used to identify network modules by applying the community Louvain algorithm, which iteratively evaluates different ways of assigning nodes to modules, in

order to maximise the resulting modularity function Q :

$$Q = \frac{1}{v^2} \sum_{ij} (w_{ij}^+ - e_{ij}^+) \delta_{M_i, M_j} - \frac{1}{v^+ + v^-} (w_{ij}^- - e_{ij}^-) \delta_{M_i, M_j} \quad (1)$$

where v is the total weight of the graph (sum of all the graph's edges), w_{ij} is the signed weight of the edge between nodes i and j , e_{ij} is the weight of an edge divided by the total weight of the graph (superscripts denote + positive and - negative edges), and δ_{M_i, M_j} is set to 1 when nodes i and j are in the same module and 0 otherwise. We performed 100 iterations for each time-resolved network with module size resolution parameter γ set at the default $\gamma = 1$.

We calculated participation coefficient and within-degree Z -score for each node using the Brain Connectivity Toolbox. Participation coefficient was calculated as:

$$P_i = 1 - \frac{M}{s-1} \left(\frac{\kappa_{is}}{k_i} \right)^2 \quad (2)$$

where κ_{is} is the strength of positive connections between node i and other nodes in module s ; k_i is the strength of all its positive connections; and M is the number of modules in the network, as identified by the modularity detection algorithm. The participation coefficient ranges between zero (no connections with other modules) and one (equal connections to all other modules). High mean participation coefficient within a network implies higher levels of integration between-modules.

The within-module degree Z -score Z_i was calculated as:

$$z_i = \frac{\kappa_{is} - \bar{\kappa}_{is}}{\sigma_{\kappa_{is}}} \quad (3)$$

where κ_{is} is the strength of connections between node i and other nodes in module s , and $\bar{\kappa}_{is}$ and $\sigma_{\kappa_{is}}$ are, respectively, the average and the standard deviation of κ_{is} over all nodes belonging to module s .

Joint histograms of participation coefficient and within-module Z -score were then derived for each time point¹² and for each participant. The cluster with the higher average participation coefficient was defined as the "Integrated" state and the cluster with the lower average participation coefficient as the "Segregated" state, as previously described^{12,18,20}. K -means clustering was then performed and assigned each dynamic functional connectivity matrix to one of two clusters (Integrated vs Segregated)^{12,18,20} (Fig. 1a). $K = 2$ clusters was also best performing in data-driven evaluation (Supplementary Fig. 1).

We calculated: (1) *proportion of time spent in each state* as the number of timepoints within each state divided by number of total timepoints(63), (2) *average dwell time* as the number of consecutive windows/timepoints belonging to each state and (3) *number of transitions* as the number of transitions from one state to the other; transitions were further divided into transitions from integrated-to-segregated and from segregated-to-integrated states.

Structural network construction. After DWI-image preprocessing, diffusion tensor metrics were calculated for each participant and constrained spherical deconvolution performed¹¹⁹ followed by anatomically constrained tractography (10 million streamlines)¹²⁰ and spherical deconvolution-informed filtering of tractograms (SIFT2)¹²¹. The resulting set of streamlines, weighted by a cross-sectional multiplier, was used to construct the structural brain network as a 232^*232 undirected weighted connectivity matrix.

Network control analysis. We examined how the structural brain network of each participant, composed of white matter tracts, constrains the brain in transitioning from one state of functional connectivity (Integrated or Segregated) to the other. To do this, we used a linear time-invariance network model, as previously detailed^{29,31,50}. This can describe neural states as simulated states (x) of a network with n nodes over time steps t using:

$$x(t+1) = Ax(t) + Bu(t) \quad (4)$$

where $x(t)$ is a vector (1^*n nodes) that represents the brain state at given time t , n is the number of nodes (232 ROIs), matrix A represents the structural connectome n^*n (normalised to ensure stability^{31,32}), matrix B is the matrix of control nodes for the network with n^*n dimensions and $u(t)$ is the control energy applied for each node at a given time t . In all analyses, we did not constrain the number of nodes that could be controlled, therefore B is an identity matrix.

This model can be used to derive the structural control energy necessary to transition from an initial state $x(0)$ to a target state $x(T)$ where $T = 1$ is the control horizon^{31,122} as:

$$\min_u \int_0^T (x_T - x(t))' S (x_T - x(t)) + \rho u(t)' t(t) dt \quad (5)$$

where x_T is the target state (1^*n vector where n is the number of nodes), S is the diagonal n^*n matrix that selects a subset of states to constrain (here the identity matrix), ρ is the importance of the input penalty to the state penalty (here $\rho = 1$) and T is the control horizon.

Importantly, this formalism does not prescribe how the initial "brain state" $x(0)$ and target state $x(T)$ are identified: both data-driven and pre-specified states have been used^{33,35}. Here, our goal is to provide a mechanistic understanding of dynamic transitions between the Integrated and Segregated states of dynamic

functional connectivity. Since the network control theory model requires each state to be represented as a 1×232 vector, we represented the *Integrated* and *Segregated* states by their sum connectivity profiles (or “connectivity density”), comprised of the sum of the connection weights (Pearson correlation coefficient) from each node to all other nodes; this was calculated separately for each state.

We then used this equation to calculate the control energy to be applied to each node of the network to: (1) transition from the integrated-to-segregated state (using x_0 (baseline state), the sum connectivity vector of the *Integrated* state; and x_T (target state), the sum connectivity vector of the *Segregated* state), (2) transition from the segregated-to-integrated state, using as x_0 the sum connectivity vector of the *Segregated* and state x_T , the sum connectivity vector of the *Integrated* state, and (3) persist within the *Integrated* or within the *Segregated* state (i.e. transition from one state to itself), using the sum connectivity vector for that state for both x_0 and x_T (Fig. 1b). A sum of the control energies to be applied across all nodes of the network represents the minimal energy for the specific transition. Thereby, minimal transition and persistence energies were calculated for each individual’s own *Integrated* and *Segregated* functional state by capitalising on the availability of both functional and structural data for each individual.

We also identified which brain regions contribute more to the transition from the *Integrated*-to-*Segregated* state (which differed between PD-VH and PD-non-VH), or which nodes require more energy to be applied to them in order to transition: high contributors to the state transition were defined as the top 20% of regions.

Statistics and reproducibility. Between-group differences in clinical characteristics and temporal properties of dynamic states were assessed using ANOVA (post hoc Tukey) or t -tests for normally distributed and Kruskal–Wallis (post hoc Dunn) or Mann–Whitney for non-normally distributed variables (normality assessed using Shapiro–Wilk test and visual inspection). Statistical significance threshold $p < 0.05$. Differences in transition and persistence energy between PD-VH vs PD-non-VH were performed using repeated measures ANOVA ($p < 0.05$).

In addition, we investigated whether each of the two states significantly differed across groups using network-based statistics (NBS)¹²³. A general linear model was used with PD-VH versus PD-non-VH and PD versus controls as contrasts of interest and age and total intracranial volume as covariates. Permutation testing with unpaired t -tests was performed (5000 permutations), calculating a test statistic for each connection. An a priori threshold of $t = 2.7$ was applied based on our sample size and family-wise error rate (FWE) of $p < 0.05$.

Correlation with Neurotransmitter systems. We investigated whether temporal changes in functional connectivity were associated with specific neurotransmitter systems (Fig. 1c). First, we calculated the regional control energy needed to transition towards and persist within a state that was more predominant in PD-VH. This was expressed as a vector 1×232 with one control energy value per node. Neurotransmitter profiles were extracted for each of the 232 ROIs from publically-available maps using JuSpace¹²⁴:

- Serotonin receptors 5-HT1A, 5-HT1B, 5-HT2A based on carbonyl-(11C)WAY-100635, [(11C)P943, [(18F)altanseri templates¹²⁵.
- D1 receptors based on the D1R-selective [(11C)SCH23390 template¹²⁶.
- D2/3 receptors based on the [(11C)raclopride template¹²⁷.
- and GABA_A receptors based on the (11C)flumazenil template¹²⁸.

Each of the templates was registered to MNI space and parcellated with the Schaefer-232 atlas and mean values of binding potential were extracted from each ROI using the built-in JuSpace function¹²⁴.

Expression profiles for genes of noradrenergic, cholinergic (nicotinic and muscarinic), dopaminergic and serotonergic receptors were obtained using data from the Allen Human Brain Atlas (AHBA)⁵², with preprocessing as recently described¹²⁹. We extracted and mapped gene expression data to the 232 ROIs of our parcellation using abagen¹³⁰. Data was pooled between homologous cortical regions to ensure adequate coverage of both left (data from six donors) and right hemisphere (data from two donors). Distances between samples were evaluated on the cortical surface with a 2 mm distance threshold. Probe-to-gene annotations were updated in Re-Annotator¹³¹. Only probes where expression measures were above a background threshold in more than 50% of samples were selected. A representative probe for a gene was selected based on highest intensity. Gene expression data were normalised across the cortex using scaled, outlier-robust sigmoid normalisation. 15,745 genes survived these preprocessing and quality assurance steps. Expression profiles for 31 pre-selected genes (Supplementary Table 2) encoding receptors for noradrenaline, acetylcholine, dopamine and serotonin were extracted for each of the 232 ROIs.

We correlated regional control energy with (1) regional receptor density profiles for serotonin (*5HT1a*, *5HT2a* and *5HT1b*), dopamine (*D1* and *D2*) and GABA receptors, and (2) regional gene expression for 31 pre-selected genes. The significance of correspondence between regional control energy and regional neurotransmitter density/gene expression was estimated using a spatial permutation test which generates randomly rotated brain maps whilst preserving spatial covariance¹³². We performed 1000 random spatial permutations¹³³ and calculated the Spearman correlation coefficient between extracted regional control energy values and neurotransmitter maps to build a null distribution. The permutation-based p -value (p_{spin}) was calculated as the proportion of times that the

null correlation coefficients were greater than the empirical coefficients^{132,133}. Derived p_{spin} values were then corrected for multiple comparisons (Benjamini Hochberg; FDR-corrected values denoted as q_{spin}).

Statistical analyses were performed in Python 3 (Jupyter Lab v1.2.6).

Reporting summary. Further information on research design is available in the Nature Research Reporting Summary linked to this article.

Data availability

Source data used to generate Figs. 2–4 are provided in Supplementary Data.

Code availability

Analysis code is available here: <https://github.com/AngelikaZa/TVFC>. Links to further data sources and packages used are found in the Supplementary Material.

Received: 31 March 2022; Accepted: 25 August 2022;

Published online: 08 September 2022

References

- Hobson, P. & Meara, J. Risk and incidence of dementia in a cohort of older subjects with Parkinson’s disease in the United Kingdom. *Mov. Disord.* **19**, 1043–1049 (2004).
- McKinlay, A. et al. A profile of neuropsychiatric problems and their relationship to quality of life for Parkinson’s disease patients without. *Dement. Park. Relat. Disord.* **14**, 37–42 (2007).
- Goetz, C. G. & Stebbins, G. T. Mortality and hallucinations in nursing home patients with advanced Parkinson’s disease. *Neurology* **45**, 669–671 (1995).
- Fox, M. D. & Raichle, M. E. Spontaneous fluctuations in brain activity observed with functional magnetic resonance imaging. *Nat. Rev. Neurosci.* **8**, 700–711 (2007).
- Muller, A. J., Shine, J. M., Halliday, G. M. & Lewis, S. J. G. Visual hallucinations in Parkinson’s disease: theoretical models. *Mov. Disord.* **29**, 1591–1598 (2014).
- Shine, J. M. et al. The role of dysfunctional attentional control networks in visual misperceptions in Parkinson’s disease. *Hum. Brain Mapp.* **35**, 2206–2219 (2014).
- Shine, J. M. et al. Imagine that: elevated sensory strength of mental imagery in individuals with Parkinson’s disease and visual hallucinations. *Proc. Biol. Sci.* **282**, 20142047 (2015).
- Yao, N. et al. The default mode network is disrupted in Parkinson’s disease with visual hallucinations. *Hum. Brain Mapp.* **35**, 5658–5666 (2014).
- Baggio, H. C., Segura, B. & Junque, C. Resting-state functional brain networks in Parkinson’s disease. *CNS Neurosci. Ther.* **21**, 793–801 (2015).
- Allen, E. A. et al. Tracking whole-brain connectivity dynamics in the resting state. *Cereb. Cortex* **24**, 663–676 (2014).
- Hutchison, R. M. et al. Dynamic functional connectivity: promise, issues, and interpretations. *NeuroImage* **80**, 360–378 (2013).
- Shine, J. M. et al. The dynamics of functional brain networks: integrated network states during cognitive task performance. *Neuron* **92**, 544–554 (2016).
- Liégeois, R. et al. Resting brain dynamics at different timescales capture distinct aspects of human behavior. *Nat. Commun.* **10**, 2317 (2019).
- Sakoğlu, U. et al. A method for evaluating dynamic functional network connectivity and task-modulation: application to schizophrenia. *Magma N. Y.* **23**, 351–366 (2010).
- Kaiser, R. H. et al. Dynamic resting-state functional connectivity in major depression. *Neuropsychopharmacology* **41**, 1822–1830 (2016).
- Jin, C. et al. Dynamic brain connectivity is a better predictor of PTSD than static connectivity. *Hum. Brain Mapp.* **38**, 4479–4496 (2017).
- Rashid, B. et al. Classification of schizophrenia and bipolar patients using static and dynamic resting-state fMRI brain connectivity. *NeuroImage* **134**, 645–657 (2016).
- Luppi, A. I. et al. Consciousness-specific dynamic interactions of brain integration and functional diversity. *Nat. Commun.* **10**, 4616 (2019).
- Luppi, A. I. et al. Brain network integration dynamics are associated with loss and recovery of consciousness induced by sevoflurane. *Hum. Brain Mapp.* **42**, 2802–2822 (2021).
- Luppi, A. I. et al. LSD alters dynamic integration and segregation in the human brain. *NeuroImage* **227**, 117653 (2021).
- Cordes, D. et al. Advances in functional magnetic resonance imaging data analysis methods using Empirical Mode Decomposition to investigate

- temporal changes in early Parkinson's disease. *Alzheimers Dement. Transl. Res. Clin. Interv.* **4**, 372–386 (2018).
22. Kim, J. et al. Abnormal intrinsic brain functional network dynamics in Parkinson's disease. *Brain J. Neurol.* **140**, 2955–2967 (2017).
 23. Díez-Cirarda, M. et al. Dynamic functional connectivity in Parkinson's disease patients with mild cognitive impairment and normal cognition. *NeuroImage Clin.* **17**, 847–855 (2018).
 24. Fiorenzato, E. et al. Dynamic functional connectivity changes associated with dementia in Parkinson's disease. *Brain* **142**, 2860–2872 (2019).
 25. Zarkali, A. et al. Fiber-specific white matter reductions in Parkinson hallucinations and visual dysfunction. *Neurology* <https://doi.org/10.1212/WNL.0000000000009014> (2020).
 26. Rau, Y.-A. et al. A longitudinal fixel-based analysis of white matter alterations in patients with Parkinson's disease. *NeuroImage Clin.* **24**, 102098 (2019).
 27. Hall, J. M. et al. Changes in structural network topology correlate with severity of hallucinatory behavior in Parkinson's disease. *Netw. Neurosci.* **3**, 521–538 (2019).
 28. Zarkali, A. et al. Differences in network controllability and regional gene expression underlie hallucinations in Parkinson's disease. *Brain* **143**, 3435–3448 (2020).
 29. Gu, S. et al. Controllability of structural brain networks. *Nat. Commun.* **6**, 1–10 (2015).
 30. Tang, E. & Bassett, D. S. Colloquium: Control of dynamics in brain networks. *Rev. Mod. Phys.* **90**, 031003 (2018).
 31. Betzel, R. F., Gu, S., Medaglia, J. D., Pasqualetti, F. & Bassett, D. S. Optimally controlling the human connectome: the role of network topology. *Sci. Rep.* **6**, 30770 (2016).
 32. Gu, S. et al. Optimal trajectories of brain state transitions. *NeuroImage* **148**, 305–317 (2017).
 33. Cornblath, E. J. et al. Temporal sequences of brain activity at rest are constrained by white matter structure and modulated by cognitive demands. *Commun. Biol.* **3**, 1–12 (2020).
 34. Braun, U. et al. Brain network dynamics during working memory are modulated by dopamine and diminished in schizophrenia. *Nat. Commun.* **12**, 3478 (2021).
 35. Cui, Z. et al. Optimization of energy state transition trajectory supports the development of executive function during youth. *eLife* **9**, e53060 (2020).
 36. Fallon, J. et al. Timescales of spontaneous fMRI fluctuations relate to structural connectivity in the brain. *Netw. Neurosci.* **4**, 788–806 (2020).
 37. Kringelbach, M. L. et al. Dynamic coupling of whole-brain neuronal and neurotransmitter systems. *Proc. Natl Acad. Sci. USA* **117**, 9566–9576 (2020).
 38. Kapur, S. Psychosis as a state of aberrant salience: a framework linking biology, phenomenology, and pharmacology in schizophrenia. *Am. J. Psychiatry* **160**, 13–23 (2003).
 39. Schmack, K., Bosc, M., Ott, T., Sturgill, J. F. & Kepecs, A. Striatal dopamine mediates hallucination-like perception in mice. *Science* **372**, eabf4740 (2021).
 40. Weiner, W. J., Koller, W. C., Perlik, S., Nausieda, P. A. & Klawans, H. L. Drug holiday and management of Parkinson disease. *Neurology* **30**, 1257–1261 (1980).
 41. Fénelon, G., Mahieux, F., Huon, R. & Ziegler, M. Hallucinations in Parkinson's disease: prevalence, phenomenology and risk factors. *Brain J. Neurol.* **123**(Pt 4), 733–745 (2000).
 42. Gallagher, D. A. et al. Testing an aetiological model of visual hallucinations in Parkinson's disease. *Brain* **134**, 3299–3309 (2011).
 43. Huot, P. et al. Increased 5-HT_{2A} receptors in the temporal cortex of parkinsonian patients with visual hallucinations. *Mov. Disord.* **25**, 1399–1408 (2010).
 44. Firbank, M. J. et al. Reduced occipital GABA in Parkinson disease with visual hallucinations. *Neurology* **91**, e675–e685 (2018).
 45. Hepp, D. H. et al. Loss of ts with Parkinson disease and visual hallucinations. *Radiology* **285**, 896–903 (2017).
 46. Shine, J. M. et al. Human cognition involves the dynamic integration of neural activity and neuromodulatory systems. *Nat. Neurosci.* **22**, 289–296 (2019).
 47. Shine, J. M. et al. Computational models link cellular mechanisms of neuromodulation to large-scale neural dynamics. *Nat. Neurosci.* **24**, 765–776 (2021).
 48. Zuberer, A. et al. Integration and segregation across large-scale intrinsic brain networks as a marker of sustained attention and task-unrelated thought. *NeuroImage* **229**, 117610 (2021).
 49. Wei, J. et al. Effects of virtual lesions on temporal dynamics in cortical networks based on personalized dynamic models. *NeuroImage* **254**, 119087 (2022).
 50. Kim, J. Z. et al. Role of graph architecture in controlling dynamical networks with applications to neural systems. *Nat. Phys.* **14**, 91–98 (2018).
 51. Onofri, M., Espay, A. J., Bonanni, L., Pizzi, S. D. & Sensi, S. L. Hallucinations, somatic-functional disorders of PD-DLB as expressions of thalamic dysfunction. *Mov. Disord.* **34**, 1100–1111 (2019).
 52. Hawrylycz, M. et al. Canonical genetic signatures of the adult human brain. *Nat. Neurosci.* **18**, 1832–1844 (2015).
 53. Aarsland, D. et al. Neuropsychiatric symptoms in patients with Parkinson's disease and dementia: frequency, profile and associated care giver stress. *J. Neurol. Neurosurg. Psychiatry* **78**, 36–42 (2007).
 54. Damaraju, E. et al. Dynamic functional connectivity analysis reveals transient states of dysconnectivity in schizophrenia. *NeuroImage Clin.* **5**, 298–308 (2014).
 55. Weber, S. et al. Dynamic functional connectivity patterns in schizophrenia and the relationship with hallucinations. *Front. Psychiatry* **11**, 227 (2020).
 56. Carhart-Harris, R. L. et al. Neural correlates of the LSD experience revealed by multimodal neuroimaging. *Proc. Natl Acad. Sci. USA* **113**, 4853–4858 (2016).
 57. Stiso, J. et al. White matter network architecture guides direct electrical stimulation through optimal state transitions. *Cell Rep.* **28**, 2554–2566.e7 (2019).
 58. Singleton, S. P. et al. LSD flattens the brain's energy landscape: evidence from receptor-informed network control theory. <https://doi.org/10.1101/2021.05.14.444193> (2021).
 59. Weil, R. S., Hsu, J. K., Darby, R. R., Soussand, L. & Fox, M. D. Neuroimaging in Parkinson's disease dementia: connecting the dots. *Brain Commun.* **1**, fcz006 (2019).
 60. Zarkali, A., McColgan, P., Leyland, L. A., Lees, A. J. & Weil, R. S. Longitudinal thalamic white and grey matter changes associated with visual hallucinations in Parkinson's disease. *J. Neurol. Neurosurg. Psychiatry*. <https://doi.org/10.1136/jnnp-2021-326630> (2021).
 61. Russo, M. et al. The pharmacology of visual hallucinations in synucleinopathies. *Front. Pharmacol.* **10**, 1379 (2019).
 62. Geyer, M. A. & Vollenweider, F. X. Serotonin research: contributions to understanding psychoses. *Trends Pharmacol. Sci.* **29**, 445–453 (2008).
 63. Deco, G. et al. Whole-brain multimodal neuroimaging model using serotonin receptor maps explains non-linear functional effects of LSD. *Curr. Biol. CB* **28**, 3065–3074.e6 (2018).
 64. Cheng, A. V. et al. Cortical serotonin-5₂ receptor binding in Lewy body dementia, Alzheimer's and Parkinson's diseases. *J. Neurol. Sci.* **106**, 50–55 (1991).
 65. Cummings, J. et al. Pimavanserin for patients with Parkinson's disease psychosis: a randomised, placebo-controlled phase 3 trial. *Lancet Lond. Engl.* **383**, 533–540 (2014).
 66. University College, London. *Trial of Ondansetron as a Parkinson's Hallucinations Treatment*. <https://clinicaltrials.gov/ct2/show/NCT04167813> (2019).
 67. Khundakar, A. A. et al. Analysis of primary visual cortex in dementia with Lewy bodies indicates GABAergic involvement associated with recurrent complex visual hallucinations. *Acta Neuropathol. Commun.* **4**, 66 (2016).
 68. Iwaki, H. et al. Genomewide association study of Parkinson's disease clinical biomarkers in 12 longitudinal patients' cohorts. *Mov. Disord.* **34**, 1839–1850 (2019).
 69. O'Callaghan, C. et al. Locus coeruleus integrity and the effect of atomoxetine on response inhibition in Parkinson's disease. *Brain* <https://doi.org/10.1093/brain/awab142> (2021).
 70. Vazey, E. & Aston-Jones, G. The emerging role of norepinephrine in cognitive dysfunctions of Parkinson's disease. *Front. Behav. Neurosci.* **6**, 48 (2012).
 71. Dahl, M. J., Mather, M., Sander, M. C. & Werkle-Bergner, M. Noradrenergic responsiveness supports selective attention across the adult lifespan. *J. Neurosci.* **40**, 4372–4390 (2020).
 72. Phillips, W. A., Larkum, M. E., Harley, C. W. & Silverstein, S. M. The effects of arousal on apical amplification and conscious state. *Neurosci. Conscious.* **2016**, niw015 (2016).
 73. Kjaerby, C. et al. Memory-enhancing properties of sleep depend on the oscillatory amplitude of norepinephrine. *Nat Neurosci* **25**, 1059–1070 (2022).
 74. Arnsten, A. F. T., Wang, M. J. & Paspalas, C. D. Neuromodulation of thought: flexibilities and vulnerabilities in prefrontal cortical network synapses. *Neuron* **76**, 223–239 (2012).
 75. Yellin, D., Berkovich-Ohana, A. & Malach, R. Coupling between pupil fluctuations and resting-state fMRI uncovers a slow build-up of antagonistic responses in the human cortex. *NeuroImage* **106**, 414–427 (2015).
 76. Jacob, S. N. & Nienborg, H. Monoaminergic neuromodulation of sensory processing. *Front. Neural Circuits* **12**, 51 (2018).
 77. Power, J. D. et al. Methods to detect, characterize, and remove motion artifact in resting state fMRI. *NeuroImage* **84**, 320–341 (2014).
 78. Saad, Z. S. et al. Trouble at rest: how correlation patterns and group differences become distorted after global signal regression. *Brain Connect* **2**, 25–32 (2012).
 79. Power, J. D., Laumann, T. O., Plitt, M., Martin, A. & Petersen, S. E. On Global fMRI Signals and Simulations. *Trends Cogn. Sci.* **21**, 911–913 (2017).
 80. Orban, C., Kong, R., Li, J., Chee, M. W. L. & Yeo, B. T. T. Time of day is associated with paradoxical reductions in global signal fluctuation and functional connectivity. *PLoS Biol.* **18**, e3000602 (2020).

81. Honey, C. J. et al. Predicting human resting-state functional connectivity from structural connectivity. *Proc. Natl Acad. Sci. USA* **106**, 2035–2040 (2009).
82. Nozari, E. et al. Is the brain macroscopically linear? A system identification of resting state dynamics. Preprint at *bioRxiv* <https://doi.org/10.1101/2020.12.21.423856> (2020).
83. Schulz, M.-A. et al. Different scaling of linear models and deep learning in UKBiobank brain images versus machine-learning datasets. *Nat. Commun.* **11**, 4238 (2020).
84. Luppi, A. I. et al. Paths to oblivion: common neural mechanisms of anaesthesia and disorders of consciousness. Preprint at *bioRxiv* <https://doi.org/10.1101/2021.02.14.431140> (2021).
85. Papapetropoulos, S. et al. A questionnaire-based (UM-PDQH) study of hallucinations in Parkinson's disease. *BMC Neurol.* **8**, 21 (2008).
86. Creavin, S. T. et al. Mini-Mental State Examination (MMSE) for the detection of dementia in clinically unevaluated people aged 65 and over in community and primary care populations. *Cochrane Database Syst. Rev.* <https://doi.org/10.1002/14651858.CD011145.pub2> (2016).
87. Dalrymple-Alford, J. C. et al. The MoCA: well-suited screen for cognitive impairment in Parkinson disease. *Neurology* **75**, 1717–1725 (2010).
88. Wechsler, D. *Wechsler Adult Intelligence Scale-Fourth Edition* (NCS Pearson, 2008).
89. Stroop, J. R. Studies of interference in serial verbal reactions. *J. Exp. Psychol.* **18**, 643–662 (1935).
90. Rende, B., Ramsberger, G. & Miyake, A. Commonalities and differences in the working memory components underlying letter and category fluency tasks: a dual-task investigation. *Neuropsychology* **16**, 309–321 (2002).
91. Warrington, E. K. *Recognition Memory Test: Manual* (UKNER-Nelson, 1984).
92. Warrington, E. K. The graded naming test: a restandardisation. *Neuropsychol. Rehabil.* **7**, 143–146 (1997).
93. Benton, A. L., Varney, N. R. & Hamsher, K. D. Visuospatial Judgment: A Clinical Test. *Arch. Neurol.* **35**, 364–367 (1978).
94. Zigmond, A. S. & Snaith, R. P. The hospital anxiety and depression scale. *Acta Psychiatr. Scand.* **67**, 361–370 (1983).
95. Goetz, C. G. et al. Movement Disorder Society-sponsored revision of the Unified Parkinson's Disease Rating Scale (MDS-UPDRS): scale presentation and clinimetric testing results. *Mov. Disord.* **23**, 2129–2170 (2008).
96. Hummel, T., Sekinger, B., Wolf, S. R., Pauli, E. & Kobal, G. 'Sniffin' sticks': olfactory performance assessed by the combined testing of odor identification, odor discrimination and olfactory threshold. *Chem. Senses* **22**, 39–52 (1997).
97. Stiasny-Kolster, K. et al. The REM sleep behavior disorder screening questionnaire—a new diagnostic instrument. *Mov. Disord.* **22**, 2386–2393 (2007).
98. Tomlinson, C. L. et al. Systematic review of levodopa dose equivalency reporting in Parkinson's disease. *Mov. Disord.* **25**, 2649–2653 (2010).
99. Esteban, O. et al. MRIQC: advancing the automatic prediction of image quality in MRI from unseen sites. *PLoS ONE* **12**, e0184661 (2017).
100. Roalf, D. R. et al. The impact of quality assurance assessment on diffusion tensor imaging outcomes in a large-scale population-based cohort. *NeuroImage* **125**, 903–919 (2016).
101. Zarkali, A. et al. Organisational and neuromodulatory underpinnings of structural-functional connectivity decoupling in patients with Parkinson's disease. *Commun. Biol.* **4**, 1–13 (2021).
102. Esteban, O. et al. fMRIPrep: a robust preprocessing pipeline for functional MRI. *Nat. Methods* **16**, 111–116 (2019).
103. Cox, R. W. AFNI: software for analysis and visualization of functional magnetic resonance neuroimages. *Comput. Biomed. Res.* **29**, 162–173 (1996).
104. Jenkinson, M., Bannister, P., Brady, M. & Smith, S. Improved optimization for the robust and accurate linear registration and motion correction of brain images. *NeuroImage* **17**, 825–841 (2002).
105. Andersson, J. L. R., Skare, S. & Ashburner, J. How to correct susceptibility distortions in spin-echo echo-planar images: application to diffusion tensor imaging. *NeuroImage* **20**, 870–888 (2003).
106. Greve, D. N. & Fischl, B. Accurate and robust brain image alignment using boundary-based registration. *NeuroImage* **48**, 63–72 (2009).
107. Behzadi, Y., Restom, K., Liu, J. & Liu, T. T. A component based noise correction method (CompCor) for BOLD and perfusion based fMRI. *NeuroImage* **37**, 90–101 (2007).
108. Tournier, J.-D. et al. MRtrix3: a fast, flexible and open software framework for medical image processing and visualisation. *NeuroImage* **202**, 116137 (2019).
109. Veraart, J., Fieremans, E. & Novikov, D. S. Diffusion MRI noise mapping using random matrix theory. *Magn. Reson. Med.* **76**, 1582–1593 (2016).
110. Kellner, E., Dhital, B., Kiselev, V. G. & Reiser, M. Gibbs-ringing artifact removal based on local subvoxel-shifts. *Magn. Reson. Med.* **76**, 1574–1581 (2016).
111. Anderson, G. Assuring quality/resisting quality assurance: academics' responses to 'quality' in some Australian universities. *Qual. High. Educ.* **12**, 161–173 (2006).
112. Tustison, N. J. et al. N4ITK: improved N3 bias correction. *IEEE Trans. Med. Imaging* **29**, 1310–1320 (2010).
113. Schaefer, A. et al. Local-global parcellation of the human cerebral cortex from intrinsic functional connectivity MRI. *Cereb. Cortex* **28**, 3095–3114 (2018).
114. Tian, Y., Margulies, D. S., Breakspear, M. & Zalesky, A. Topographic organization of the human subcortex unveiled with functional connectivity gradients. *Nat. Neurosci.* **23**, 1421–1432 (2020).
115. Luppi, A. I. & Stamatakis, E. A. Combining network topology and information theory to construct representative brain networks. *Netw. Neurosci.* **5**, 96–124 (2021).
116. Messé, A. Parcellation influence on the connectivity-based structure–function relationship in the human brain. *Hum. Brain Mapp.* **41**, 1167–1180 (2020).
117. Fukushima, M. et al. Structure–function relationships during segregated and integrated network states of human brain functional connectivity. *Brain Struct. Funct.* **223**, 1091–1106 (2018).
118. Rubinov, M. & Sporns, O. Weight-conserving characterization of complex functional brain networks. *NeuroImage* **56**, 2068–2079 (2011).
119. Hollander, T., Raffelt, D. & Connelly, A. In *ISMRM Workshop on Breaking the Barriers of Diffusion MRI* Vol. 5 (ISMRM, 2016).
120. Smith, R. E., Tournier, J.-D., Calamante, F. & Connelly, A. Anatomically-constrained tractography: improved diffusion MRI streamlines tractography through effective use of anatomical information. *NeuroImage* **62**, 1924–1938 (2012).
121. Smith, R. E., Tournier, J.-D., Calamante, F. & Connelly, A. SIFT2: enabling dense quantitative assessment of brain white matter connectivity using streamlines tractography. *NeuroImage* **119**, 338–351 (2015).
122. Zöllner, D. et al. Structural control energy of resting-state functional brain states reveals less cost-effective brain dynamics in psychosis vulnerability. *Hum. Brain Mapp.* **42**, 2181–2200 (2021).
123. Zalesky, A., Fornito, A. & Bullmore, E. T. Network-based statistic: identifying differences in brain networks. *NeuroImage* **53**, 1197–1207 (2010).
124. Dukart, J. et al. JuSpace: a tool for spatial correlation analyses of magnetic resonance imaging data with nuclear imaging derived neurotransmitter maps. *Hum. Brain Mapp.* **42**, 555–566 (2021).
125. Savli, M. et al. Normative database of the serotonergic system in healthy subjects using multi-tracer PET. *NeuroImage* **63**, 447–459 (2012).
126. Kaller, S. et al. Test-retest measurements of dopamine D1-type receptors using simultaneous PET/MRI imaging. *Eur. J. Nucl. Med. Mol. Imaging* **44**, 1025–1032 (2017).
127. Alakurtti, K. et al. Long-term test-retest reliability of striatal and extrastriatal dopamine D2/3 receptor binding: study with [(11)C]raclopride and high-resolution PET. *J. Cereb. Blood Flow. Metab.* **35**, 1199–1205 (2015).
128. Dukart, J. et al. Cerebral blood flow predicts differential neurotransmitter activity. *Sci. Rep.* **8**, 4074 (2018).
129. Arnatkeviciūtė, A., Fulcher, B. D. & Fornito, A. A practical guide to linking brain-wide gene expression and neuroimaging data. *NeuroImage* **189**, 353–367 (2019).
130. Markello, R., Shafiei, G., Zheng, Y.-Q. & Mišić, B. abagen: a toolbox for the Allen Brain Atlas genetics data. *Zenodo* <https://doi.org/10.5281/zenodo.3726257> (2020).
131. Arloth, J., Bader, D. M., Röh, S. & Altmann, A. Re-annotator: annotation pipeline for microarray probe sequences. *PLoS ONE* **10**, e0139516 (2015).
132. Alexander-Bloch, A. et al. On testing for spatial correspondence between maps of human brain structure and function. *NeuroImage* **178**, 540–551 (2018).
133. Váša, F. et al. Adolescent tuning of association cortex in human structural brain networks. *Cereb. Cortex* **28**, 281–294 (2018).

Acknowledgements

We thank all our participants for their time. We gratefully acknowledge the support of NVIDIA Corporation with the donation of the Quadro P6000 GPU used for this research. The authors acknowledge the use of the UCL Myriad High Performance Computing Facility (Myriad@UCL), and associated support services, in the completion of this work. This research was also supported by the National Institute for Health Research University College London Hospitals Biomedical Research Centre. A.Z. is supported by an Alzheimer's Research UK Clinical Research Fellowship (2018B-001). P.M.C. is supported by the National Institute for Health Research. R.S.W. is supported by a Wellcome Clinical Research Career Development Fellowship (205167/Z/16/Z).

Author contributions

Study design and concept: A.Z. and R.W., data collection: A.Z., L.A.L. and R.W., imaging and statistical analysis: A.Z., drafting and revision of the manuscript: A.Z., P.M.C., L.A.L., A.L., S.R., E.S., A.J.L. and R.W.

Competing interests

R.S.W. has received honoraria from GE Healthcare and Britannia. The other authors declare no competing interests.

Additional information

Supplementary information The online version contains supplementary material available at <https://doi.org/10.1038/s42003-022-03903-x>.

Correspondence and requests for materials should be addressed to Angeliki Zarkali.

Peer review information *Communications Biology* thanks Shi Gu and the other, anonymous, reviewer(s) for their contribution to the peer review of this work. Primary Handling Editors: Zhijuan Qiu. Peer reviewer reports are available.

Reprints and permission information is available at <http://www.nature.com/reprints>

Publisher's note Springer Nature remains neutral with regard to jurisdictional claims in published maps and institutional affiliations.



Open Access This article is licensed under a Creative Commons Attribution 4.0 International License, which permits use, sharing, adaptation, distribution and reproduction in any medium or format, as long as you give appropriate credit to the original author(s) and the source, provide a link to the Creative Commons license, and indicate if changes were made. The images or other third party material in this article are included in the article's Creative Commons license, unless indicated otherwise in a credit line to the material. If material is not included in the article's Creative Commons license and your intended use is not permitted by statutory regulation or exceeds the permitted use, you will need to obtain permission directly from the copyright holder. To view a copy of this license, visit <http://creativecommons.org/licenses/by/4.0/>.

© The Author(s) 2022